Journal of the European Ceramic Society 41 (2021) 5548–5557

Contents lists available at ScienceDirect

Journal of the European Ceramic Society

journal homepage: www.elsevier.com/locate/jeurceramsoc

Reactive SPS for sol–gel alumina samples: Structure, sintering behavior, and mechanical properties

Pedro Rivero-Antúnez [a,b], Rafael Cano-Crespo [a], Florentino Sánchez-Bajo [c], Arturo Domínguez-Rodríguez [a], Víctor Morales-Flórez [a,b,*]

[a] Departamento de Física de la Materia Condensada, Universidad de Sevilla, 41012, Sevilla, Spain
[b] Instituto de Ciencia de Materiales de Sevilla, Centro Mixto CSIC-Universidad de Sevilla, 41092 Sevilla, Spain
[c] Departamento de Física Aplicada, Escuela de Ingenierías Industriales, Universidad de Extremadura, Avda de Elvas s/n, 06006 Badajoz, Spain

ARTICLE INFO

Keywords:
Reactive SPS sintering
α-Al_2O_3
Boehmite
Fracture toughness
Vickers hardness

ABSTRACT

This work presents a fast and direct controlled routine for the fabrication of fully dense alumina based on the reactive spark plasma sintering (reactive-SPS) of boehmite (γ-AlOOH) nano-powders obtained by the sol–gel technique. The evolution of the transition aluminas during sintering has been studied. Some boehmite powders were seeded with α-Al_2O_3 particles prior to the gelation. Boehmite seeded powders exhibited a direct transition to α-Al_2O_3 at 1070 °C, enhancing the transformation kinetics and lowering the required temperature by more than 100 °C. For comparison, other samples were prepared by previously annealing the seeded and unseeded boehmite powders. Thus, α-Al_2O_3 powders were obtained and were sintered by standard-SPS. A detailed structural and mechanical characterization is presented, comparing the hardness and indentation fracture resistance for different grain sizes and porosities. Both the reactive-SPSed samples and the standard-SPSed samples showed a high hardness (18–20 GPa), whereas the reactive-SPSed samples exhibited a lower indentation fracture resistance due to a large grain size (~10 μm). Improvements of this procedure for obtaining smaller grain size are discussed. In summary, the presented technique brings a revolutionary fast method for the fabrication of fully dense alumina, as this process reduces the time and temperature required for alumina densification.

1. Introduction

The fabrication of ceramic matrix composites reinforced by the inclusion of carbon allotropes has been hindered by severe synthesis difficulties such as the proper dispersion of the reinforcing agents. With the purpose of finding the best route for the homogeneous inclusion of carbon allotropes, such as carbon nanotubes, or graphene nanoplatelets inside alumina matrix composites, and to achieve a significant increase of the fracture toughness of the material, the sol–gel route based on aluminum alkoxides or hydroxides, such as boehmite (γ-AlOOH), has been considered a promising procedure [1–3]. The sol–gel method allows the dispersion of the secondary phase in a large liquid volume, the starting sol, where the use of techniques such as the addition of surfactants or the application of ultrasound dissociates the CNTs bundles or GNP agglomerations. Then, the rapid controlled gelation [4] leads to the formation of a solid network and avoids the re-aggregation of the dispersed carbon allotropes. At the same time, the sol–gel method might promote the intragranular location of the nanotubes inside the alumina grains [1,2,5,6].

It has been verified that a previous annealing of boehmite powders at 600 °C transforms boehmite into γ-Al_2O_3 (see Fig. 1), and the introduction of γ-Al_2O_3 (theoretical density = 3.65 g/cm^3 [7]) powders into the SPS inhibited the correct densification during the subsequent spark plasma sintering (SPS) [3], even though the conditions were sufficient for sintering comercial α-Al_2O_3 powders [8–10]. Nevertheless, those results have motivated the research of an optimized way for sintering fully dense alumina samples from boehmite nanopowders. A potential way to achieve 100% dense samples is to increase the temperature of the previous annealing to 1200 °C, which ensures the total transformation of boehmite into α-Al_2O_3, with the consequent benefits for the later

* Corresponding author at: Department of Condensed-Matter Physics, University of Seville, P.O. 1065, 41080 Seville, Spain.
E-mail addresses: privero@us.es (P. Rivero-Antúnez), racacres@us.es (R. Cano-Crespo), fsanbajo@unex.es (F. Sánchez-Bajo), adorod@us.es (A. Domínguez-Rodríguez), vmorales@us.es (V. Morales-Flórez).
URL: http://grupo.us.es/fqm393/ (V. Morales-Flórez).

https://doi.org/10.1016/j.jeurceramsoc.2021.04.060
Received 30 December 2020; Received in revised form 1 April 2021; Accepted 30 April 2021
Available online 5 May 2021

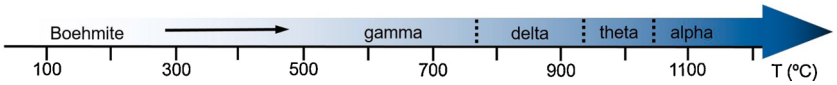

Fig. 1. Evolution of metastable alumina polymorphs (also known as transition aluminas) from boehmite (γ-aluminum oxyhydroxide). Based on data from Ref. [12].

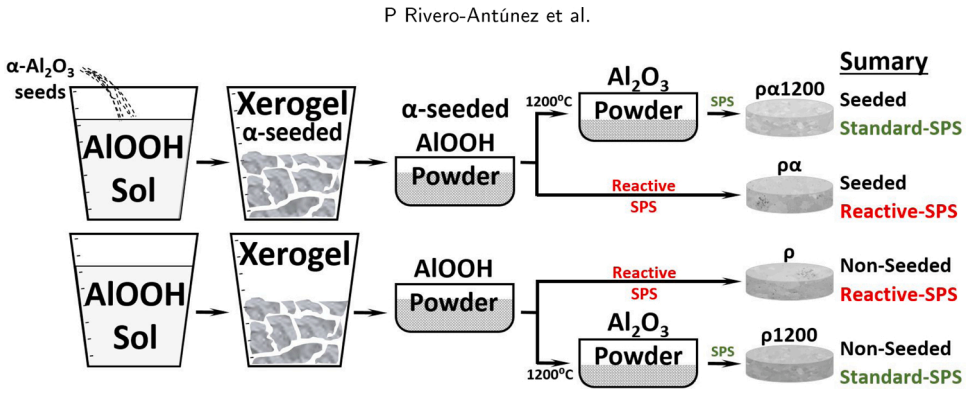

Fig. 2. Sketch summarizing the path followed for each sample. In the last column, the details of each of the four types of samples considered in this work are listed.

sintering. However, one of the major features of SPS is its ability for a fast densification of the sample versus conventional methods like hot pressing, or pressureless sintering, which require several hours for the total densification of ceramics. Given the costs of time and resources involved in the calcination of boehmite powders at 1200 °C for obtaining α-Al_2O_3 powders, the suggestion of the direct sintering of boehmite without the previous annealing step is a remarkably captivating idea. In addition, the particle size of the boehmite precursor powders is known to be below 10 nm which may enhance the compaction of the powders and promote a small grain size of the final alumina. According to Prof. J. A. Hedvall's studies on solid-state chemistry [11] published in 1938, this kind of sintering is known as reactive sintering, based on the enhanced reactivity of solids during their decomposition or phase transformation.

Boehmite is an aluminium oxyhydroxide, one of the polymorphs of monohydrated aluminas ($Al_2O_3{\cdot}H_2O$). Boehmite presents an orthorhombic structure of layered deformed octahedra with the aluminum ion close to its center, where the $[AlO_6^{9-}]$ octahedra share one edge and the hydroxyl ions hold the layers by hydrogen bonds. Its theoretical density is 3.01 g/cm^3 [13]. The dehydroxylation reaction of boehmite yields alumina and water:

$$2AlO(OH) \rightarrow Al_2O_3 + H_2O \quad (1)$$

Taking advantage of this reaction, other authors have tried the reactive-sintering route before to obtain dense alumina, but usually with other more time-consuming sintering procedures, such as hot pressing [14–17], cold-pressing [18,19], or pressureless sintering [20]. Using the reactive-SPS procedure has only been tried once before, by Zaman et al. [21], at 1600 °C, a much higher temperature than the one used in the present work. Despite obtaining high density alumina, their work did not highlight the concept of the reactive sintering route based on the SPS technique (reactive-SPS) as an encouraging feature for efficient sintering of dense alumina.

In this work, we explore the performance of a new reactive-SPS route in which the reaction and full densification occur together at lower temperatures. To do so, we use the strategy of seeding the transformation process to enhance the formation of a required phase. Although it is a resource extensively used, it was hardly improved until the 80's [20,22]. The idea is that the α-Al_2O_3 seeds will act as nucleation sites so lowering the transformation temperatures of the final α-Al_2O_3 and preventing the formation of the vermicular structure due to the phase transformation of boehmite, reducing the residual porosity [23,24] with the additional help of high pressure. Furthermore, the kinetics of the reactive-SPS processes are discussed and compared with the results obtained by conventional SPS routes (namely, standard-SPS). Structural characterization has been performed at different scales, and the mechanical properties have been measured at different applied loads.

2. Materials and methods

2.1. Sample synthesis

A route based on the works of Kumagai and Messing [20,23] and Barrera-Solano et al. [25] was employed for the preparation of the powders. In Fig. 2, the synthesis procedure is summarized. A boehmite sol (*Nyacol Nano Technologies, Inc.*, density = 1.14 g/cm^3, pH = 3.5) was slowly seeded with α-Al_2O_3 seeds (30–40 nm particle size, 99% purity), supplied by *NanoAmor, Inc.* The amount of seeds was chosen in such a way that the mass represented 2 wt.% of the final α-Al_2O_3.

After 24 h of vigorous magnetic stirring, the seeded sol was gelled by adding $NH_3^{(aq)}$ (*PanReac*, pH = 11.6), until the pH of the sol reached a value of 6.0, approximately, and a rapid gelation occurred. Another set of samples was obtained by exactly the same procedure but without the addition of α-Al_2O_3 seeds. The gels were dried in a stove for 48 h at 40 °C. After that, the resulting xerogels were grinded in an agate mortar and sieved (<212 μm), obtaining white boehmite powders. At this stage, two different samples were present: the unseeded boehmite powders (named ρ, "rho"), and the boehmite powders seeded with α-Al_2O_3 (named $\rho\alpha$, "rho-alpha"). Part of each powder was directly considered for reactive-SPS, and the rest was annealed at 1200 °C in a tubular furnace with an argon atmosphere, resulting in α-Al_2O_3 powder according to the expected sequence of thermal transformations of aluminum hydroxides into alumina polymorphs [12] (see Fig. 1). The calcined unseeded boehmite powder was named ρ1200, and the seeded one, $\rho\alpha$1200. These annealed powders were submitted to conventional standard-SPS. In summary, the samples with α-Al_2O_3 seeds ("seeded samples") include the character α; those sintered via conventional SPS are labeled with the suffix "1200", i.e., ρ1200 and $\rho\alpha$1200, and will be referred as "standard-SPSed samples"; the samples sintered via reactive-SPS are ρ and $\rho\alpha$, and will be referred as "reactive-SPSed samples". For the sake of clarity, the types of samples considered in this work are summarized in Fig. 2.

For all cases, the samples were sintered in a *Dr. Sinter Lab, Inc.*, model

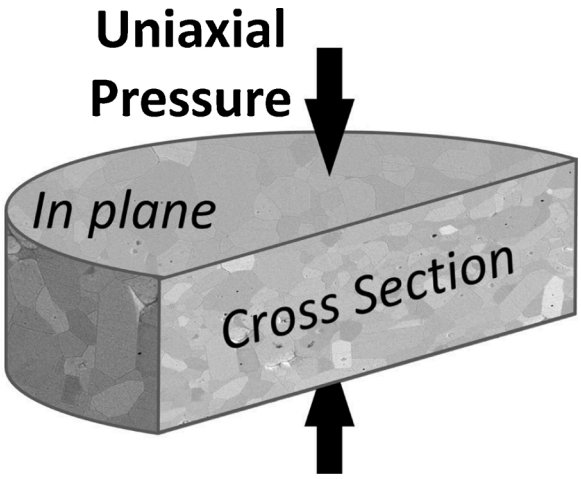

Fig. 3. Scheme of a SPSed sample showing in plane (ip) and cross section (cs) surfaces.

515S (Kanagawa, Japan), at 1300 °C for a dwell time of 5 min (heating ramp: 100 °C/min, cooling ramp: 50 °C/min), applying 75 MPa of constant uniaxial pressure and a squared pulse of current (12 s on and 2 s off). These parameters were chosen because they have previously been successfully used for fully densifying commercial pure α-Al_2O_3 powders [8–10,26]. During the sintering, the piston travel (shrinkage) and the temperature of the graphite die were recorded. The temperature was measured with a pyrometer which was capable of obtaining data from 570 °C onwards. The temperature was measured in the exterior wall of the graphite die which might present a time-lag in the automatic temperature adjustment. This was clear when the temperature reached 1300 °C and the thermal inertia overheated the sample by a few degrees Celsius.

The sintered samples were prepared by the classical ceramographics methods, i.e., the "*RCEP*" protocol [3], namely: rectifying, cutting, embedding, and polishing (up to 1 μm diamond slurry), so obtaining polished surfaces for the measurement of micro-structural and mechanical properties. In order to research the anisotropic effects due to the uniaxial compression, two different surfaces were *rcepped* for each sample: the "in plane" surface (ip), perpendicular to the pressure axis, and the "cross section" surface (cs), parallel to this axis (see Fig. 3).

2.2. Chemical and structural characterization

The chemical composition of the samples was analyzed with an X-ray fluorescence (XRF) spectrometer (*Panalytical* model AXIOS). The crystallographic structures of the samples were investigated by XRD (X-ray powder diffraction), using a *Bruker* diffractometer model D8I-90, by the step-scanning technique with a range from $2\theta = 10°$ to 120°, step of $\Delta\theta = 0.015°$, counting time of 0.5 s, using Cu-K_α radiation ($K_{\alpha1} + K_{\alpha2}$ doublet) with no monochromator, 40 kV, 30 mA, and sample rotating at 30 rpm.

For the study of the nanostructural features of the powders, samples were degassed under an N_2 flux at 150 °C for 2 h and analyzed by N_2 physisorption (*Micromeritics* ASAP2010), working at 77 K with a resolution of 10^{-4} mm Hg. The specific surface areas (*SSA*) of the powders were obtained using the curves of gas adsorption and desorption, and the BET model [27]. The micro- and nanostructure were also examined by scanning electron microscopy with SEMFEG, *Hitachi* model S5200 and *FEI* model Teneo, with acceleration voltages of 5 and 2 kV, respectively. Transmission electron microscopy (TEM, *Philips* model CM-200) was also employed. To measure grain size the grain boundaries must be revealed, so the sintered monolithic samples were exposed to a thermal etching of 15 min at 1200 °C (heating ramp: 5 °C/min) in an alumina tubular furnace in the presence of an inert argon atmosphere at constant flux. After the etching treatment, dozens of SEM micrographs were analyzed with the help of *ImageJ* software [28] (typically, more than 300 grains per surface were studied for the statistics).

Thermogravimetric analyses (TGA) and differential scanning calorimetry (DSC) in flowing air were conducted to evaluate the chemical evolution of samples when they were heated. TGA procedures were performed in a STD Q600 (*TA Instruments*), heating a few milligrams of powder samples at 10 °C/min from room temperature up to 1000 °C, under an air flux of 100 mL/min. Mass losses received special attention in the thermal range corresponding to the dehydroxylation of the boehmite (200–450 °C).

The densities of the monolithic samples were obtained by the Archimedes' method, submerging the cut pieces of the monolithic samples into distilled water at 25 °C. A set of 5 samples was considered for each type of sample for the statistics.

2.3. Surface topographic characterization

To quantify the quality of the polishing of the sintered samples, the roughness is an important value to be considered when measuring mechanical properties [29]. In all the final surfaces, the average arithmetic roughness in the surface, S_a, was measured. This magnitude is defined as the arithmetic mean of the absolute value of the height z from the average plane of the surface σ of area A:

$$S_a = \frac{1}{A}\iint_{\sigma} |z(x,y)| \ \mathrm{dx} \ \mathrm{dy} \tag{2}$$

The topography of the surfaces was obtained using an 3D optical-confocal microscope-interferometer (*Sensofar* S-NEOX) and the *SensoMaps* software. The surfaces were photographed with an optical microscope (model Leica DMRE, *Leica Microsystems GmbH*, Germany). A magnification of 50× was employed with a gaussian filter of 80 μm. For the values of S_a, fifteen different selected areas were studied for each surface. Deeper analyses of the quality of the polishing and other parameters quantifying the roughness from the measurement of $z(x, y)$, such as S_q, a quadratic treatment analogous to the arithmetic average S_a can be found in the Supplementary Material, Table SM1. This extended discussion includes five different selected areas, and from each area fifteen parallel lines (profiles), and another fifteen parallel lines perpendicular to the first, were used to calculate the values of R_a and R_q. Consequently, 30 values for each magnitude were obtained for the same area, that is, 150 values for each examined sample.

2.4. Mechanical characterization

The characterization of the hardness was based on Vickers indentation tests at several loads (0.5 to 10 kp) and 10 s of dwell, repeating the test at least ten times for statistical analysis. The tests were performed in a *Buehler Wilson* VH1150 MicroVickers Hardness Tester and a *Struers* Duramin. The applied force:area ratio of the print gives the hardness, H, of the material. The fracture toughness, K_{Ic}, was estimated from the indentation fracture resistance, K_{IFR}, a value obtained from the Vickers Indentation Fractures (VIF) method, and using the Shetty's equation for median type cracks:

$$K_{\mathrm{IFR}} = 0.023(E/H)^{1/2} P \Big/ c^{3/2} \tag{3}$$

where E is the elastic modulus, H is the Vickers hardness, P is the applied load, and c is the length of the crack, measured from the center of the print. More detailed aspects of the equation are given in [30]. We chose this equation after Miyazaki et al. [31,32] proved that, for fully dense alumina ceramics, this equation provides values of K_{IFR} absolutely correlated with values of K_{Ic} obtained by standard methods, such as SEPB.

The indentation prints and the length of the cracks were measured using an optical microscope with a ×20/0.40 objective, a CCD camera

Table 1
BET specific surface area of powders, and estimated spherical diameter of the powder particles calculated from SSA. Number of measured grains for the characterization of the grain size on both surfaces, in plane (ip) and cross section (cs). Uncertainties are one standard deviation. Relative densities of sintered samples of the studied materials.

Sample name	BET SSA (m^2/g)	Estimated diameter (nm)	Measured grains	Grain size (μm)		Relative density (%)
				ip	cs	
ρ	163.5	6.0	1002	30 ± 13	24 ± 12	99.6 ± 1.7
$\rho\alpha$	156.5	6.3	916	12 ± 7	10 ± 6	99.4 ± 1.9
ρ1200	5.4	140	563	1.3 ± 0.9	1.5 ± 1.0	95.3 ± 0.6
$\rho\alpha$1200	4.7	160	891	1.3 ± 0.8	1.3 ± 1.1	98.9 ± 1.4

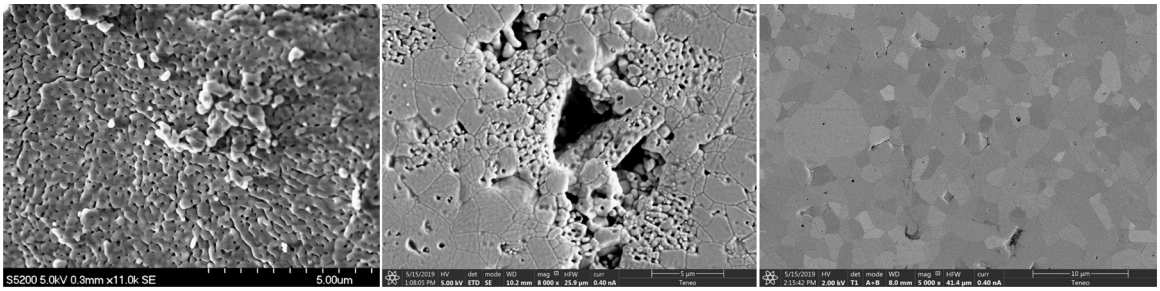

Fig. 4. Left: ρ1200 sample at powder stage (prior to sintering). **Center**: cross section surface of standard-SPSed sample ρ1200, illustrating the persistence of vermicular structure after sintering, yielding to inter- and intragranular porosities. A hole, probably due to grain chipping during the rectifying and polishing, crowns the center of the image. **Right**: image of the sample $\rho\alpha$1200-ip revealing the fully dense structure of the grains.

with digital zoom, and a traveling stage, as a good optical resolution is a crucial feature for reliable values of K_{IFR} obtained by VIF tests [32]. Finally, after mechanical characterization, SEM was used again to explore the nano- and microstructure of the polished surfaces of the samples, the indentation prints, and the morphology of the cracks.

3. Results and discussion

3.1. Chemical and structural characterization

First of all, the precursor powders of all the types of samples were characterized. The XRF analyses revealed that the composition of all the powders was 98.5% Al in mass, and the rest consisted of impurities of Mg (0.6%), Na (0.2%), Si (0.2%), Ti (0.1%), Fe (0.1%), and Zr (<0.1%). This composition remained mostly the same after the SPS.

The specific surface area (*SSA*) values from the nitrogen physisorption experiments performed on the powders are listed in Table 1. With these data we can obtain a first estimation of the size of the particles of the precursor powder, using a simple first-approach model based on spherical particles:

$$\mathrm{SSA} = \frac{\mathrm{surface}}{\mathrm{mass}} = \frac{4\pi R^2}{\delta \frac{4}{3}\pi R^3} \rightarrow D = 2R = \frac{6}{\delta \cdot \mathrm{SSA}}, \quad (4)$$

where R and D are the radius and the diameter of the spherical particles, respectively, and δ is the theoretical bulk density of the powder. Boehmite powders exhibited an SSA of 163.5 m^2/g, which involves an estimated particle size of 6.0 nm. Although this approximation underestimates the real size, the results are in accordance with the particles sizes observed using TEM and SEM. Boehmite powders are composed of nanoparticles of dimensions around 7 × 30 nm (see TEM image in Supplementary Material Fig. SM2), that are arranged in clusters of nanoparticles with a wide range of sizes [5]. On the other hand, the addition of 2 wt.% of α-Al_2O_3 seeds, which have an SSA of 9.0 m^2/g, gave to $\rho\alpha$ powders a quite smaller SSA, and, consequently, a larger estimated particle size.

Regarding the calcined powders for standard-SPS, as expected, they exhibited much lower values of SSA than the non-calcined powders. Moreover, sample ρ1200 presented a smaller particle size than $\rho\alpha$1200 as the $\rho\alpha$1200 powders contained a 2 wt.% of α-Al_2O_3 seeds when they were calcined at 1200 °C to transform boehmite into alumina, leading to an enhanced crystallization. The inspection of the calcined powders with electron microscopy showed that the powder samples ρ1200 and $\rho\alpha$1200 have much larger characteristic sizes than the estimated particle sizes of 140 or 160 nm, respectively. That difference is principally explained by nanometric vermicular structure of the calcined ρ1200 powder, typically found in α-Al_2O_3 obtained from the thermal evolution of transition aluminas (see Fig. 4-left).

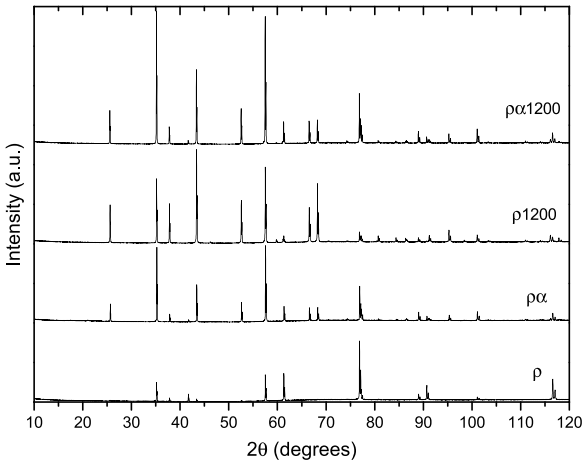

Fig. 5. Diffractograms of the sintered samples.

The crystallographic characterization of the powders has already been reported [3,5] and clearly showed the expected patterns of boehmite for the non-calcined sample, and α-Al_2O_3 for the seeded non-calcined and all the calcined ones. Fig. 5 shows the diffraction patterns of the sintered samples. The peaks displayed in the diffractograms correspond to the X-ray diffraction lines of the α-Al_2O_3, showing that all the samples (reactive-SPSed and standard-SPSed, and with or without α-Al_2O_3 seeds) have the same composition. Nevertheless, relative intensities are very different from the ideal structure of α-Al_2O_3 for

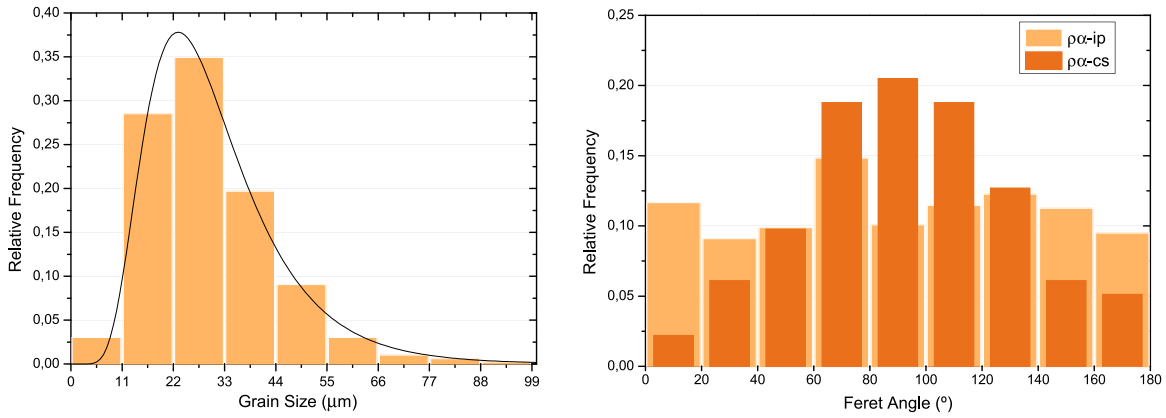

Fig. 6. Left: histogram of the grain size for ρ sample in the ip surface (ρ-ip), which follows a log-normal distribution (fitting curve, see equation (2)). This is true on both ip and cs surfaces for every sample. **Right**: in the ip surface of all the samples, the grains do not show any preferential orientation, and a flat distribution is obtained in the histogram number of grains (relative frequency) vs. Feret angle. Alternatively, anisotropic distribution of Feret angle is obtained in the cross section of the sample, indicating the preferential grain growth in the plane perpendicular to the uniaxial pressure direction. Data obtained from $\rho\alpha$-ip and $\rho\alpha$-cs surfaces of sample $\rho\alpha$.

the ρ sample. In this case, possible texture or preferred orientation effects can be responsible of this behavior. The rest of the samples show relative intensities similar to the ideal case. Therefore, the theoretical density of full-dense pure α-Al_2O_3, 3.985 g/cm^3 [7,13] was considered as the reference value for the measurement of the densities of the sintered samples (Table 1). Relative densities above 99.4% were found for the reactive-SPSed samples, while 95.3% and 98.9% were found for samples ρ1200 and $\rho\alpha$1200, respectively. According to Delesse's principle of stereology, the fraction of area of pores observed in SEM images was the same as the fraction of volume occupied by that porosity. Thus, the lower density of sample ρ1200 is in agreement with the remaining vermicular porosity observed on its surface (as shown in Fig. 4-right, and discussed below).

A qualitative inspection of the X-ray diffraction peaks shows that these are very narrow (Fig. SM3), displaying the doublet components even at low angles ($2\theta < 40°$). This indicates that microstructural effects – especially domain size – are very small in all samples. This can be assessed by measuring the breadths of the peaks. In this way, we have fitted Voigt functions to the peaks with heights greater than 1000 counts, calculating their corresponding Cauchy (β_C) and Gauss (β_G) integral breadths. In most cases, the fit was very good, providing Goodness-of-Fit values around 1–2. As an example, Fig. SM4 shows the fit of a Voigt function to the 006 peak of the ρ sample. Fig. SM5 displays the Cauchy and Gauss integral breadths for the analyzed samples as function of the peak position. Note that, Gaussian integral breadths are similar (for a particular angular position) for the four samples, whereas Cauchy integral breadths are similar for the samples ρ, $\rho\alpha$, and $\rho\alpha$1200, being greater for the sample ρ1200.

Classical microstructural analysis by X-ray diffractometry, especially with respect to the estimation of domain size, is restricted to domain sizes in the nanometric scale. Therefore, domain sizes of about 1 μm and greater cannot be reliably determined, because the widths of the experimental and instrumental-spectral (used as standard) peaks are very similar. This similarity indicates that the experimental line-broadening is mainly due to instrumental-spectral effects, being microstructural effects very small or negligible. In regards to this, shape parameter errors are of the order of the difference between the widths of the experimental and instrumental-spectral peaks and this leads to unacceptable uncertainties.

However, in our case, as the reactive-SPSed samples ρ and $\rho\alpha$ seem to have grain sizes of about tens of microns, we have considered the possibility to estimate the domain size of the samples ρ1200 and $\rho\alpha$1200 (considering ρ as standard for the sample ρ1200, and $\rho\alpha$ for the sample $\rho\alpha$1200). Assuming that the domain size effect is approximated by the Cauchy component of the microstructural profile, only the ρ1200 sample can be analyzed, because the Cauchy integral breadths of the $\rho\alpha$1200 sample are the same (within of the uncertainties) that the corresponding to the $\rho\alpha$ sample. In the case of the ρ1200 sample, a classical analysis using the Williamson-Hall plot [33] and the Warren-Averbach method [34] provide a mean apparent volume domain size of 1.3 ± 0.8 μm, and a mean apparent area domain size of 0.7 ± 0.3 μm, with a root mean square strain of $(1.2 \pm 0.2)\cdot 10^{-4}$. In summary, the domain size values, in spite of the noticeable uncertainties (as we have pointed out above), are in rough agreement with the value derived from the electron microscopy. Note that this suggest that nanometric sub-grains are not present in the ρ1200 sample, as the mean values of the domain sizes are about 1 μm. A similar result could be considered for the sample $\rho\alpha$1200 because no significant differences appear between the breadths of the peaks and those corresponding to the sample $\rho\alpha$, used as standard.

3.2. Surface characterization

The SEM study of the sintered samples allowed the estimation of the typical grain sizes (Table 1). A significant difference was observed between the reactive samples, with typical grain sizes larger than 10 μm (as observed in Figs. SM6, SM7 and SM8), and the standard-SPS ones, with grain sizes lower than 1.5 μm (Fig. 4-center and -right), one order of magnitude smaller. These results are validated by the estimates of crystallite domain size obtained by X-ray diffractometry, discussed previously. In addition, in Fig. 4-center, the SEM image of sample ρ1200 shows some details of its microstructure that helps to explain its low density. It can be confirmed that the structure is not totally closed and some residual porosity remains, mainly due to the vermicular network observed in the precursor powder (Fig. 4-left) that persisted when α-Al_2O_3 is made by the evolution of transition aluminas [20]. In Fig. 4-right, an image of the sample $\rho\alpha$1200-ip reveals the fully dense structure of the grains, with unusual intragranular porosity. Regarding the reactive-SPSed samples, another relevant result is that the grain size of non-seeded sample ρ, is twice the grain size of the seeded sample $\rho\alpha$. This fact could be explained given the absence of nucleation sites in sample ρ, what enables a larger grain growth: grain boundaries have more time to expand before they meet another grain boundary. On the contrary, $\rho\alpha$ has a much larger density of nucleation sites so grain growth is limited by meeting faster grain boundaries.

The statistical analysis of the grain sizes reveals that the grain size (random variable D which takes values d) follows the classically reported log-normal random distribution [35,36] (see Fig. 6-left), whose probability density function is given by:

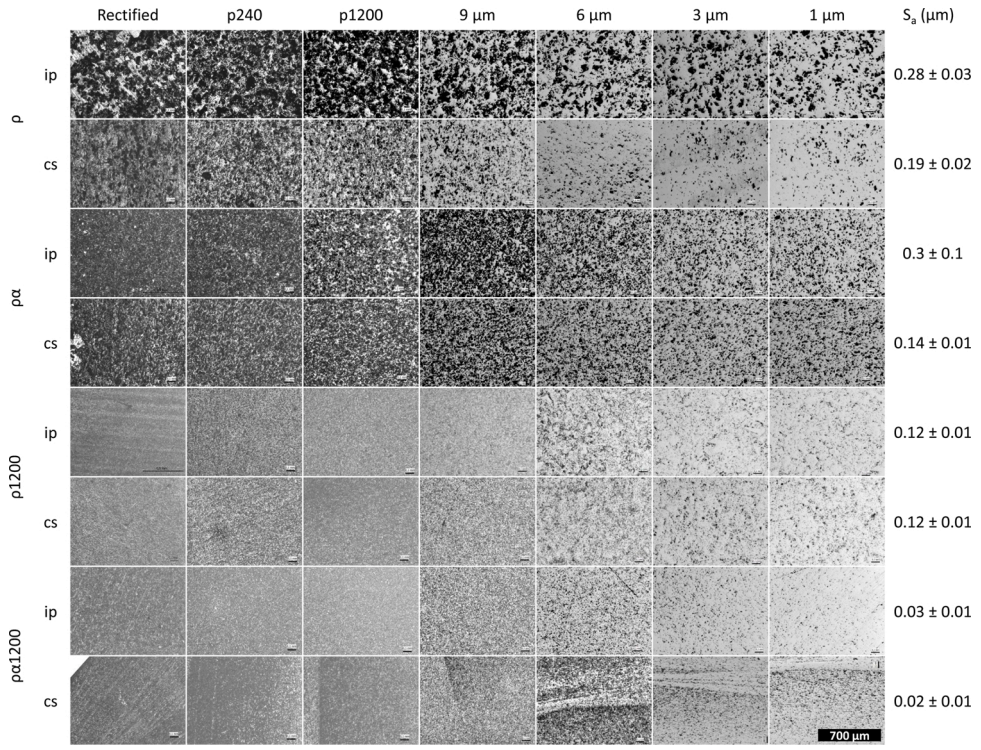

Fig. 7. Evolution of surfaces after the different polishing steps. In plane (ip) and cross section (cs) surfaces are shown, as well as average measured roughness (S_a). A 3D reconstruction of the polished surface of the sample ρ obtained by confocal microscopy is shown in Supplementary Material Fig. SM1.

$$f_{\mu,\sigma}(d) = \frac{1}{d\sigma\sqrt{2\pi}} exp\left(-\frac{[\ln(d) - \mu]^2}{2\sigma^2} \right) \quad (5)$$

where μ and σ are the mean and the standard deviation of the variable's natural logarithm. Note that they are not the expectation and standard deviation of random variable D, as D is defined as $D = exp(\mu + \sigma Z)$, where Z is a random variable normally distributed. The arithmetic mean values of D for the different samples (i.e. $\overline{d}$, not μ) are listed as the characteristic grain sizes in Table 1. Additionally, the typical anomalous alumina grain growth [36] was present and is responsible for the relatively large uncertainties of the central values. This behavior is probably enhanced by the tendency for boehmite to grow in a preferred direction, leading to the formation of high aspect ratio alumina crystals [19,37], a process that starts, in the case of the conventionally sintered samples, all along the pre-annealing of boehmite powders at 1200 °C.

The preferential direction of grain growth was quantified by the Feret diameter: it is defined as the maximum diameter that can be drawn between any two points of the boundary of a grain, i.e., the maximum caliper. The Feret angle is then the angle between the Feret diameter and an arbitrary fixed direction. In this work, for the cross section surfaces, the fixed direction to measure the Feret angle was the pressure axis. For the in plane surfaces, the selected direction is any radial direction perpendicular to the loaded axis. All the ip surfaces showed an isotropic distribution of grains (see Fig. 6-right). On the other hand, the cs surfaces of samples ρ, $\rho\alpha$, and $\rho\alpha$1200 presented anisotropies (Fig. 6-right, Figs. SM6 and SM8), that is, during the sintering, the grain growth was inhibited in the direction of the applied pressure. Hence, the grains grew preferentially in the plane perpendicular to the pressure axis [38]. Surprisingly, this phenomenon was not observed at any surface (nor ip nor cs) of the sample ρ1200 sintered by conventional SPS. This may be explained by the absence of α-Al_2O_3 seeds which promoted a retarded formation of grains, and a consequent lack of time for the grains to develop in a preferential direction. Some authors [39] have suggested that what really inhibits the grain growth is the electric field, which could happen during SPS, as the electric field is applied uniaxially in the same direction as the mechanical load. Nevertheless, is a controversial topic under debate [40,41], and more experiments will be performed in order to elucidate what plays the fundamental role in the inhibition of grain growth.

During the *RCEP* procedure, the evolution of the surfaces presented significant differences between the reactive-SPSed samples and the standard ones. In Fig. 7, the surfaces were photographed with an optical microscope as the successive sandpapers and diamond slurries were used, from the coarsest p240 sandpaper to finest 1 µm diamond paste. Besides, the results of the topographic characterization of the final polished surfaces present a clear difference between the reactive-SPSed sample and the standard ones.

The higher roughness of the ρ and $\rho\alpha$ samples (up to one order of magnitude higher) is attributed to their larger grain size (Table 1) combined with the effect of grain chipping produced during the rectifying and rougher first steps of polishing. Thus, when a grain is chipped out from the surface of a reactive-SPSed sample, the "hole" left by the grain is deeper than in the standard samples. Moreover, some differences between the in plane surfaces (ip) and the cross sections ones (cs) have been appreciated. This fact may be explained attending to how the residual tensions are accumulated in the sintering process, due to anisotropic application of pressure. It is easier for a grain to be chipped out from an ip surface than from a cs surface, as the uniaxial pressure is applied perpendicularly to the ip surfaces, and larger residual tensions are accumulated *under* grains in ip surfaces, i.e., at the perpendicular plane to the axis of load. Thus, densities do not play the fundamental role determining the roughness of the samples when comparing the reactive-SPSed samples and standard samples. Nevertheless, some effects of density on the roughness can be appreciated when comparing standard samples: $\rho\alpha$1200, with a density of 98.9%, shows a smoother surface than ρ1200, with a density of 95.3% (S_a = 0.03 µm and S_a = 0.12 µm, respectively), despite the fact that both samples have the same micrometric grain size.

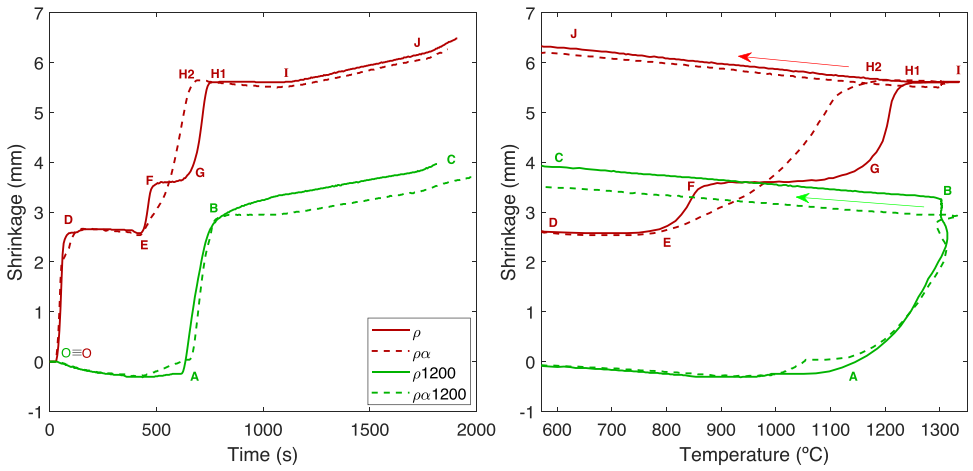

Fig. 8. Shrinkage vs. time (left) and vs. temperature (right) curves of the four different samples. Same legend corresponds to both plots. The arrows in the right panel show the direction of the process. Letters indicate similar states (shrinkage, time and temperature) on both figures. Observe that points **O** and **O** cannot be represented in the right plot, as the pyrometer can only measure the temperature above 570 °C. Note that reactive samples exhibited significant shrinkage before temperature data could be acquired, and this causes apparent shifting in Fig. 8-right. (For interpretation of the references to color in the text, the reader is referred to the web version of this article.)

3.3. Sintering and structural characterization

During the SPS, the temperature (T), and the displacement of the pistons (i.e., the shrinkage of the sample, z) were recorded. We took $z = 0$ after the 75 MPa of uniaxial pressure was applied, at room temperature. These are the points **O** and **O** in Fig. 8-left. Observe that these points cannot be represented in z vs. T in Fig. 8-right, given that the pyrometer can only measure temperatures above 570 °C.

The sintering behavior of the conventionally sintered samples, ρ1200 and $\rho\alpha$1200, can be discussed by the real-time collected shrinkage and temperature data, as shown in Fig. 8 (green lines, solid and dashed, respectively). The corresponding sintering curves z vs. t, in Fig. 8-left, show the classic densifying process of alumina powders revealed by the sample shrinkages, which start around $t = 600$ s ($T = 1150$ °C), and exhibits the maximun slopes at 1220 °C (step from points **A** to **B**). Although both samples, ρ1200 and $\rho\alpha$1200, were basically α-Al_2O_3, the better densification of the seeded one ($\rho\alpha$1200) with respect to the non-seeded one (ρ1200), is revealed by the existence of a plateau during the dwell time at maximum temperature (around $t = 700$ s to 1000 s) in sample $\rho\alpha$1200, while sample ρ1200 exhibits continuous shrinking. This could be attributed to its increased crystallization during the direct transformation of boehmite into α-Al_2O_3 in the previous pre-annealing process thanks to the presence of the seeds, and which also prevents the presence of vermicular structures in the powders and in the sintered sample $\rho\alpha$1200. This difference has been previously reported for a sintering based on pressureless sintering and hot pressing by Kumagai et al. [20,23], using much longer times at higher temperatures. Finally, during the cooling ramp (50 °C/min), beyond $t = 1000$ s, the shrinkage is produced by the linear thermal contraction (from point **B** to point **C**).

The slight difference in the sintering behavior between ρ1200 and $\rho\alpha$1200 once the maximum temperature was reached (at point **B**) can be better visualized in the plot of z vs.T, in Fig. 8-right. While the sample ρ1200 continued densifying (vertical increase of z) during the dwell time at $T = 1300$ °C, the seeded sample $\rho\alpha$1200 has already densified completely (no variation on z at maximum T). Afterwards, the cooling process from **B** to **C** performs the expected linear behavior of thermal contraction. In fact, this linearity could be used to calculate the linear thermal expansion/contraction coefficient, α_L, however, for these measurements to be made, the whole system must be calibrated, correcting the plots with the expansion of the die and pistons assembly during heating and cooling, both with and without any powder material, as suggested by Chaklader et al. [14] for hot pressing sintering.

At this point, it is interesting to highlight the differences between the described standard samples and the reactive-SPSed samples. The curve z vs. t of the ρ sample, without α-alumina seeds, (solid red line in Fig. 8-left) shows a three-step process. Firstly, from room temperature (**O**) to a temperature below 570 °C (**D**), the shrinkage reveals that the boehmite dehydroxilates and turns into γ-Al_2O_3, loosing mass in the form of H_2O during topotactic transformations (i.e., the crystal structure transforms without destruction of the original crystal morphology [20]). The transformation is consistent with the TGA and DSC results performed on boehmite ρ powders (not shown, available in Supplementary Material, Fig. SM9), and this transition is completed at 500 °C, in agreement with the irreversible evolution of alumina polymorphs (Fig. 1). The second densifying step occurs between points **E** and **F**, during which the transition alumina γ-Al_2O_3 turns into α-Al_2O_3. In the third step, from **G** to **H1**, the α-Al_2O_3 densifies, with a maximum slope at 1200 °C. From **H1** to **I**, we observe a little *plateau*, at which the sample ρ does not suffer compaction. At the end, the linear thermal contraction happens, from **I** to **J**.

Correspondingly, the inspection of the curve of z vs. T of the sample ρ (solid red line in Fig. 8-right) gives additional relevant information about the sintering behavior, specially at the highest temperatures. At the segment **H1-I**, the temperature rises up from 1250 °C to 1300 °C, is held for 5 min at 1300 °C, and goes back to 1250 °C (back to **H1**), exhibiting a linear behavior. This is a period of time in which the structure suffers an unnecessary grain growth [9], as it was revealed in the grain size measurements (>10 μm, Table 1), which will lead to a decrease in the mechanical properties. This stretch is useless from the point of view of efficient use of time and resources. At the end, the linear thermal contraction happens, from **H1** to **J**, with exactly the same slope that the standard-SPSed samples exhibited (segment from **B** to **C** of the green lines in Fig. 7).

Finally, the last curves to be analyzed, correspond to the reactive-SPSed samples $\rho\alpha$, seeded at the sol stage with α-Al_2O_3 (red dashed curve in Fig. 8-left and right). During the initial step from **O** to **D**, the dehydroxylation happens and the boehmite transforms into alumina, as the non-seeded sample ρ did. However, given that $\rho\alpha$ contains α-Al_2O_3 seeds, the boehmite turns directly into α-Al_2O_3 because of the effect of nucleation and subsequent growth [20,42]. Thus, this sample does not exhibit the step **E-F-G**. Instead, it jumps directly from **E** to **H2**, a step in which the alumina densifies. This process mimics the way that α-Al_2O_3 does in standard samples from **A** to **B**. Interestingly, this step, with a maximum slope at 1070 °C, finishes at 1200 °C at **H2**, more than a minute before **H1** and **B**. The plot of z vs. T (Fig. 8-right) confirms that the full densification (point **H2**) at a temperature 50 °C lower. Subsequently, and similarly to the red solid line of sample ρ, the bounce **H2-I-H2** is a *plateau* in which the sample does not densify any further, a segment of heating ramp, holding, and cooling, which can be considered a waste of time and energy in which the grain size grows [9]. This is confirmed by

Table 2
Vickers Hardness (HV) and Fracture Indentation Resistance (K_{IFR}) measured at different loads: 0.5, 1.0, 5.0, and 10 kp. Tests performed in plane (ip) and cross section (cs) surfaces. Uncertainties are given by one standard deviation.

Sample name (relative density)		HV0.5		HV1		HV5		HV10	
		HV (GPa)	K_{IFR} (MGf)	HV (GPa)	K_{IFR} (MGf)	HV (GPa)	K_{IFR} (MGf)	HV (GPa)	K_{IFR} (MGf)
ρ (99.6%)	ip	18.3 ± 1.2	3.0 ± 0.7	–	–	–	–	–	–
	cs	–	–	16.7 ± 1.4	2.5 ± 0.6*	–	–	–	–
$\rho\alpha$ (99.4%)	ip	16.9 ± 0.7	–	–	–	–	–	–	–
	cs	17.9 ± 1.0	–	16.1 ± 1.1	–	–	–	–	–
ρ1200 (95.3%)	ip	–	–	15.1 ± 1.4	5.0 ± 0.6	13.3 ± 0.8	5.4 ± 0.9	13.4 ± 0.5	4.4 ± 0.8
	cs	17.8 ± 1.1	–	16.7 ± 1.2	5.8 ± 0.4	14.2 ± 0.5	5.8 ± 1.0	14.4 ± 0.5	5.8 ± 1.2
$\rho\alpha$1200 (98.9%)	ip	19.7 ± 0.5	–	19.4 ± 0.8	5.0 ± 0.5	–	–	16.8 ± 0.8	5.2 ± 0.6
	cs	–	–	18.4 ± 1.2	3.7 ± 0.5	–	–	16.5 ± 0.3	4.4 ± 0.7

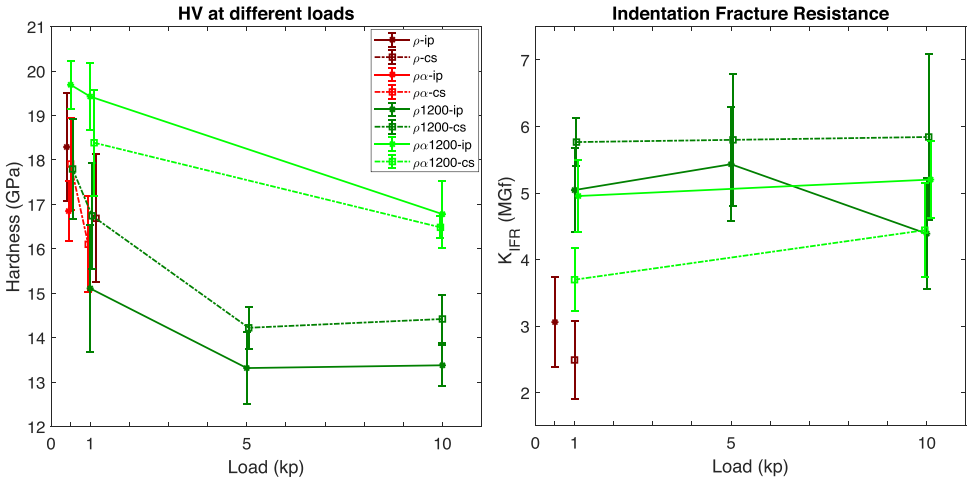

Fig. 9. Left: Vickers Hardness of different samples at several loads, illustrating Indentation Size Effect. Error bars are one standard deviation. **Right**: Indentation Fracture Resistance of samples for different loads. Error bars are one standard deviation. Points have been slightly horizontally shifted so the error bars do not overlap. Legend is the same for both graphics.

the large grain size observed in this sample (>10 μm, Table 1). Finally, the process ends up exactly as all the other samples, with the same linear thermal contraction from **H2** to **J**.

There are many factors that explain the advantages of the reactive and the standard-SPSed samples in comparison to the standard-SPSed samples, namely, a reduction of time and temperature required for the total densification of alumina. The fundamental role in the densification mechanism is being played by the ability of the particles to rearrange

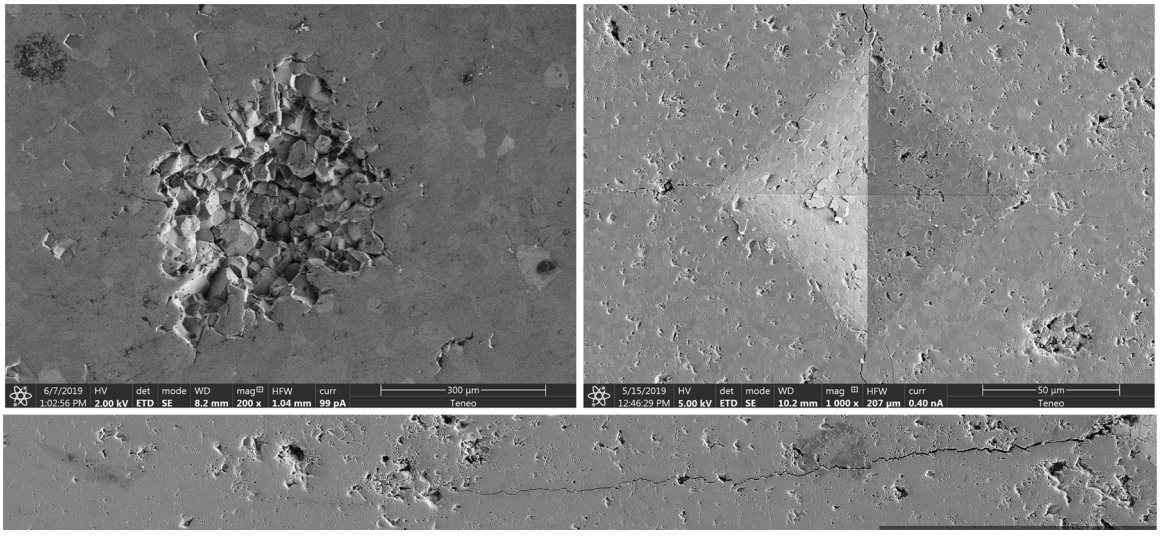

Fig. 10. Top-left: indentation HV10 on a reactive-SPSed sample (ρ-ip). **Top-right**: indentation HV10 on standard-SPSed sample (ρ1200-ip). Notice the difference on scale bars. **Bottom**: (Highly *zoom-able* image) HR-SEM image of a fracture after a HV10 indentation on the cross section surface sample ρ1200-cs, coated with 9 nm of carbon for avoiding SEM electronic charging. Scale: the black rectangle at the bottom is 70 μm long. Fracture propagation from a HV10 Vickers indentation tip along its extremely long, approximately 225 μm. This indentation was not considered either in the statistics of hardness, nor K_{IFR}. Both intergranular and transgranular crack propagation modes are present. Porosity due to vermicular remnants, grain boundaries, and holes produced by grain chipping can also be observed.

during the transformation phase [42]. During the initial application of pressure, the compaction involves a large scale particle rearrangement and motion. The smaller nanometric particle size of boehmite powders of the reactive-SPSed samples, compared with micrometric α-Al_2O_3 calcined powders of the standard-SPSed samples, induces a better initial compaction, leading to a better contact between the particles and a subsequent faster densification, as can be confirmed by the lower times and temperatures of points **H1** and **H2** in comparison to point **B**. Note that, the reactivity of boehmite powders is enhanced by its high SSA (see Table 1), 30 times bigger than the SSA of calcined alumina powders. In addition, the advantages of seeding the reaction with α-Al_2O_3 seeds are also clear as it facilitates a faster and cooler full densification. Finally, it is evident that the sintering parameters can be improved for reactive-SPS as the final segment of the process that led to excessive grain growth should be avoided. Thus, once the full density (end of shrinkage) is achieved, the process can be terminated. Probably, more parameters such as the heating ramp, cooling ramp, or the applied pressure, can be tuned and optimized to minimize the costs of alumina sintering.

3.4. Hardness and indentation fracture resistance

The monolithic samples were indented in their polished surfaces, and the obtained results of hardness and K_{IFR} are shown in Table 2 and plotted in Fig. 9. The first particular result is that, given the large grain size of reactive-SPSed samples, it was a hard task to obtain a well-defined print after indentation tests at loads larger than 1 kp. Even applying low loads, such as 0.5 and 1 kp, the prints usually had blurry edges and dozens of measurements were discarded. The grain size of these fully dense samples, larger than 10 μm, is synonymous with more brittle ceramics, i.e., the larger the grain size, the worse K_{IFR}, although not necessarily worse K_{Ic}, calculated by other methods, as reported by Yasuda et al. [43]. The energy applied by the tip is released leading to, in these cases, a multitude of radial cracks, material pile-up, and catastrophic grain chipping, as shown in Fig. 10-left when a load of 10 kp was applied. In contrast, the more fine-structured samples fabricated by standard-SPS, can be indented and measured without a hitch (Fig. 10-right).

In Fig. 9-left, it can be seen that all the samples show a hardness between 17 GPa and 20 GPa when a load of 0.5 kp is applied, 20 GPa being the value typically reported for fully dense α-Al_2O_3 [44,45]. The sample ρ1200, which did not completely densify, exhibits a lower hardness for every load tested, especially when compared with its fully dense analogous,$\rho\alpha$1200. This is due to the presence of 5% of porosity and the consequent lack of full connection of the whole crystalline microstructure [46].

On the other hand, the indentation fracture resistances measured in these set of samples (Fig. 10-right) were more sensitive to the grain size than the measured hardness, and the reactive-SPSed samples (with grain size above 10 μm) showed K_{IFR} values significantly lower than the standard-SPSed samples (around 3 MGf[1] and 5 MGf, respectively). Moreover, the indentations made on both surfaces of the samples, cs and ip, yielded no relevant differences nor any systematic trend in the hardness and K_{IFR} values. Even so, all the results are contained in the wide range of fracture toughness reported for dense pure alumina, from 2.2 to 5.7 MGf [47,48].

Regarding the measurement of cracks, defined cracks were only found in the samples with large grain size when low loads were used. The problem, then, is the difficulty to accurately measure the tiny, short cracks produced when low loads are applied. Given the huge efforts needed to obtain well defined prints and cracks even at low loads, K_{IFR} was measured in only two surfaces of one of the reactive-SPSed samples: HV-0.5 on ρ-ip, and HV-1 on ρ-cs, while the rest of reactive surfaces have been tested several times to confirm that they respond in the same way than their homologous do under the same loads. Respecting the mode of propagation of cracks, we found out that both transgranular and intergranular modes are present, with a preponderance of the latter one, as shown in Fig. 10-bottom. Finally, the indentation size effect [3,29,49], a source of discrepancy when the results of hardness are compared between different studies, is not apparently a crucial issue affecting the K_{IFR}, as deduced from Fig. 9 and the data in Table 2.

[1] Based on Prof. C. Ramadas and Mr. A. R. Jadhav's suggestion, the use of the unit "griffith" (Gf) is proposed in substitution of the awkward classical magnitude Pa · $m^{1/2}$, where 1 Gf = 1 Pa · $m^{1/2}$, as a tribute to the mechanical engineer Alan Arnold Griffith (1893–1963), as already considered in ref. [3]. Griffith was known in the field of fracture mechanics for his pioneering studies on the nature of stress and failure due to crack propagation in brittle materials.

4. Conclusions

The proposed reactive-SPS process has been explored as an efficient route for the fabrication of fully dense α-Al_2O_3, starting from a low-cost precursor such as the boehmite sol. It has been demonstrated that the fully dense samples can be obtained faster and at lower temperatures (1200 °C) than starting from α-Al_2O_3 powder. However, Vickers hardness of the obtained samples are among the highest reported for fully dense α-Al_2O_3, being affected by the density and the indentation size effect, as expected, but they are independent of the sintering route. On the contrary, indentation fracture resistance is clearly affected by the sintering route as the conditions used in the reactive-SPS produced excessive grain growth, a crucial feature affecting the fragility of the samples, leading to poor values of K_{IFR}. Nevertheless, it has been shown that this process can be optimized, avoiding the holding time and reducing the maximum temperature, and subsequently avoiding excessive grain growth.

In addition, seeding the initial sol of boehmite with α-Al_2O_3 has been proved as a key feature for optimizing the process, as it allows the direct transformation into α-Al_2O_3, lowering temperatures and times required for the full densification of samples via SPS. In this regard, a highly exciting route is to use a sol made of diaspore (α-AlOOH) nanoparticles instead of boehmite (γ-AlOOH), which would avoid transition aluminas as the diaspore transforms directly to the stable α-Al_2O_3 phase by dehydroxylation [12,50], which could simplify the process and further reduce the temperature for a complete reactive sintering and total densification of alumina.

Conflict of interest

The authors declare no conflict of interest.

Declaration of Competing Interest

The authors report no declarations of interest.

Acknowledgments

Project PGC2018-094952-B-I00 funded by FEDER/Ministerio de Ciencia e Innovación – Agencia Estatal de Investigación and project P12-FQM-1079 from Junta de Andalucía and funding support to FQM393 from Junta de Andalucía are acknowledged. V. M-F. thanks the grant from V Plan Propio de Investigación de la Universidad de Sevilla. P. R-A acknowledge European Social Fund, Empleo Juvenil European Plan and project PGC2018-094952-B-I00 from FEDER/*Ministerio de Ciencia e Innovación – Agencia Estatal de Investigación*. F.S-B. acknowledges the support provided by a project co-financed by the European Regional Development Fundand the Junta de Extremadura (GR18081). The help from the technical staff from the *CITIUS* and José Hidalgo are acknowledged, as well as the fruitful discussions with Dr. Camilo Zamora-Ledezma. The authors would like to thank the work by the National Institutes of Health, USA for the development of the *ImageJ*

software. *Comercial Química Massó* is also acknowledged for supplying the boehmite precursor Nyacol®.

Appendix A. Supplementary data

Supplementary data associated with this article can be found, in the online version, at https://doi.org/10.1016/j.jeurceramsoc.2021.04.060 .

References

[1] C.B. Mo, S.I. Cha, K.T. Kim, K.H. Lee, S.H. Hong, Fabrication of carbon nanotube reinforced alumina matrix nanocomposite by sol–gel process, Mater. Sci. Eng. A 395 (2005) 124–128.

[2] M.K. Satam, L. Gurnani, S. Vishwanathe, A. Mukhopadhyay, Development of carbon nanotube reinforced bulk polycrystalline ceramics with intragranular carbon nanotube reinforcement, J. Am. Ceram. Soc. 99 (2016) 2905–2908.

[3] P. Rivero-Antúnez, R. Cano-Crespo, L. Esquivias, N. de la Rosa-Fox, C. Zamora-Ledezma, A. Domínguez-Rodríguez, V. Morales-Flórez, Mechanical characterization of sol–gel alumina-based ceramics with intragranular reinforcement of multiwalled carbon nanotubes, Ceram. Int. 46 (2020) 19723–19730.

[4] M. Piñero, M.M. Mesa-Díaz, D. de los Santos, M.V. Reyes-Peces, J.A. Díaz-Fraile, N. de la Rosa-Fox, L. Esquivias, V. Morales-Florez, Reinforced silica-carbon nanotube monolithic aerogels synthesised by rapid controlled gelation, J. Sol–Gel Sci. Technol. 86 (2018) 391–399.

[5] L. Esquivias, P. Rivero-Antúnez, C. Zamora-Ledezma, A. Domínguez-Rodríguez, V. Morales-Flórez, Intragranular carbon nanotubes in alumina-based composites for reinforced ceramics, J. Sol–Gel Sci. Technol. 90 (2019) 162–171.

[6] V. Verma, S.C. Galaveen, L. Gurnani, T. Venkateswaran, A. Mukhopadhyay, Development of oxidation resistant and mechanically robust carbon nanotube reinforced ceramic composites, Ceram. Int. 46 (2020) 21784–21789.

[7] I. Levin, D. Brandon, Metastable alumina polymorphs: crystal structures and transition sequences, J. Am. Ceram. Soc. 81 (1998) 1995–2012.

[8] R. Cano-Crespo, B. Malmal Moshtaghioun, D. Gómez-García, A. Domínguez-Rodríguez, R. Moreno, High-temperature creep of carbon nanofiber-reinforced and graphene oxide-reinforced alumina composites sintered by spark plasma sintering, Ceram. Int. 43 (2017) 7136–7141.

[9] J.G. Santanach, A. Weibel, C. Estourns, Q. Yang, C. Laurent, A. Peigney, Spark plasma sintering of alumina: study of parameters, formal sintering analysis and hypotheses on the mechanism(s) involved in densification and grain growth, Acta Mater. 59 (2011) 1400–1408.

[10] Z. Shen, M. Johnsson, Z. Zhao, M. Nygren, Spark plasma sintering of alumina, J. Am. Ceram. Soc. 85 (2002) 1921–1927.

[11] J.A. Hedvall, Reaktionsfähigkeit fester Stoffe, 1st ed., Leipzig, J.A. Barth, 1938 https://doi.org/10.1002/bbpc.19380440414.

[12] P. Souza-Santos, H. Souza-Santos, S. Toledo, Standard transition aluminas. Electron microscopy studies, Mater. Res. 3 (2000) 104–114.

[13] F. Cardarelli, Materials Handbook, 2nd ed., Springer London, London, 2008 https://doi.org/10.1007/978-1-84628-669-8.

[14] A.C.D. Chaklader, R.C. Cook, Kinetics of reactive hot-pressing of clays and hydroxides, Am. Ceram. Soc. Bull. 47 (1968) 712–716.

[15] D.I. Matkin, W. Munro, T.M. Valentine, The fabrication of α-alumina by reactive hot-pressing, J. Mater. Sci. 6 (1971) 974–980.

[16] P.A. Badkar, J.E. Bailey, H.A. Barker, Sintering behaviour of boehmite gel, in: G. C. Kuczynski (Ed.), Sintering and Related Phenomena, 1 st ed., Springer US, Boston, MA, 1973, pp. 311–321, https://doi.org/10.1007/978-1-4615-8999-0_27.

[17] A.C.D. Chaklader, Reactive hot-pressing of aluminas, J. Am. Ceram. Soc. 61 (1978) 252–257.

[18] C. Bousquet, C. Elissalde, C. Aymonier, M. Maglione, F. Cansell, J.M. Heintz, Tuning Al2O3 crystallinity under supercritical fluid conditions: effect on sintering, J. Eur. Ceram. Soc. 28 (2008) 223–228.

[19] A.C. Zaman, C.B. Üstündag, C. Kaya, Boehmite derived surface functionalized carbon nanotube-reinforced macroporous alumina ceramics, J. Eur. Ceram. Soc. 30 (2010) 2525–2531.

[20] M. Kumagai, G.L. Messing, Controlled transformation and sintering of a boehmite Sol–Gel by α-alumina seeding, J. Am. Ceram. Soc. 68 (1985) 500–505.

[21] A.C. Zaman, C.B. Üstündag, A. Çelik, A. Kara, F. Kaya, C. Kaya, Carbon nanotube/boehmite-derived alumina ceramics obtained by hydrothermal synthesis and spark plasma sintering (SPS), J. Eur. Ceram. Soc. 30 (2010) 3351–3356.

[22] R. Bauer, Process for Production of Alpha Alumina Bodies by Sintering Seeded Boehmite Made From Alumina Hydrates, 1987.

[23] M. Kumagai, G.L. Messing, Enhanced densification of boehmite sol–gels by α-alumina seeding, J. Am. Ceram. Soc. 67 (1984) c230–c231.

[24] A.C. Zaman, C.B. Üstündag, N. Kuskonmaz, F. Kaya, C. Kaya, 3-D micro-ceramic components from hydrothermally processed carbon nanotube-boehmite powders by electrophoretic deposition, Ceram. Int. 36 (2010) 1703–1710.

[25] C. Barrera-Solano, L. Esquivias, G.L. Messing, Effect of preparation conditions on phase formation, densification, and microstructure evolution in La-β-Al2O3/Al2O3 composites, J. Am. Ceram. Soc. 82 (1999) 1318–1324.

[26] R. Cano-Crespo, P. Rivero-Antúnez, D. Gómez-García, R. Moreno, A. Domínguez-Rodríguez, The possible detriment of oxygen in creep of alumina and zirconia ceramic composites reinforced with graphene, Materials 14 (2021) 1–17.

[27] S. Brunauer, P.H. Emmett, E. Teller, Adsorption of gases in multimolecular layers, J. Am. Chem. Soc. 60 (1938) 309–319.

[28] C.A. Schneider, W.S. Rasband, K.W. Eliceiri, NIH image to ImageJ: 25 years of image analysis, Nat. Methods 9 (2012) 671–675.

[29] M.M. Renjo, L. Ćurković, D. Ćorić, Influence of surface roughness of alumina ceramics on indentation size, Mater. Test. 56 (2014) 32–39.

[30] D.K. Shetty, A.R. Rosenfield, W. Duckworth, Analysis of indentation crack as a wedge-loaded half-penny crack, J. Am. Ceram. Soc. 68 (1985). C-65–C-67.

[31] H. Miyazaki, Y.I. Yoshizawa, Correlation of the indentation fracture resistance measured using high-resolution optics and the fracture toughness obtained by the single edge-notched beam (SEPB) method for typical structural ceramics with various microstructures, Ceram. Int. 42 (2016) 7873–7876.

[32] H. Miyazaki, Y. Yoshizawa, A reinvestigation of the validity of the indentation fracture (IF) method as applied to ceramics, J. Eur. Ceram. Soc. 37 (2017) 4437–4441.

[33] G.K. Williamson, W.H. Hall, X-ray line broadening from filed aluminium and wolfram, Acta Metall. 1 (1953) 22–31.

[34] B.E. Warren, B.L. Averbach, The effect of cold-work distortion on X-ray patterns, J. Appl. Phys. 21 (1950) 595–599.

[35] S.H. Neher, H. Klein, W.F. Kuhs, Determination of crystal size distributions in alumina ceramics by a novel X-ray diffraction procedure, J. Am. Ceram. Soc. 101 (2018) 1381–1392.

[36] I. Nettleship, R.J. McAfee, W.S. Slaughter, Evolution of the grain size distribution during the sintering of alumina at 1350°C, J. Am. Ceram. Soc. 85 (2002) 1954–1960.

[37] J. Zhang, F. Shi, J. Lin, S.Y. Wei, D. Chen, J.M. Gao, Z. Huang, X.X. Ding, C. Tang, Nanoparticles assembly of boehmite nanofibers without a surfactant, Mater. Res. Bull. 43 (2008) 1709–1715.

[38] B. Ratzker, A. Wagner, S. Kalabukhov, S. Samuha, N. Frage, Non-uniform microstructure evolution in transparent alumina during dwell stage of high-pressure spark plasma sintering, Acta Mater. 199 (2020) 469–479.

[39] J.A. Bejarano-Palma, B.M. Moshtaghioun, F.L. Cumbrera-Hernández, D. Gómez-García, Motrice Forces Involved in the Grain Growth of Ceramics Under Electric Fields Applied During Spark Plasma Sintering, 2020. https://congreso2020.secv.es/wp-content/uploads/2020/10/IP05142-OV-JA.Bejarano-LVIICongr201013-1936.pdf.

[40] G. Lee, E.A. Olevsky, C. Manière, A. Maximenko, O. Izhvanov, C. Back, J. McKittrick, Effect of electric current on densification behavior of conductive ceramic powders consolidated by spark plasma sintering, Acta Mater. 144 (2018) 524–533.

[41] Z. Trzaska, A. Couret, J.P. Monchoux, Spark plasma sintering mechanisms at the necks between TiAl powder particles, Acta Mater. 118 (2016) 100–108.

[42] C. Legros, C. Carry, P. Bowen, H. Hofmann, Sintering of a transition alumina: effects of phase transformation, powder characteristics and thermal cycle, J. Eur. Ceram. Soc. 19 (1999) 1967–1978.

[43] K. Yasuda, J. Tatami, K. Asada, Y. Matsuo, S. Kimura, Influence of crack propagation path on the fracture toughness of polycrystalline Al2O3, J. Ceram. Soc. Jpn. Int. ed. 101 (1993) 1349–1355.

[44] M.H. Bocanegra-Bernal, C. Dominguez-Rios, J. Echeberria, A. Reyes-Rojas, A. Garcia-Reyes, A. Aguilar-Elguezabal, Spark plasma sintering of multi-, single/double- and single-walled carbon nanotube-reinforced alumina composites: is it justifiable the effort to reinforce them? Ceram. Int. 42 (2016) 2054–2062.

[45] I. Ahmad, H. Cao, H. Chen, H. Zhao, A. Kennedy, Y.Q. Zhu, Carbon nanotube toughened aluminium oxide nanocomposite, J. Eur. Ceram. Soc. 30 (2010) 865–873.

[46] N. Miyazaki, T. Hoshide, Influence of porosity and pore distributions on strength properties of porous alumina, J. Mater. Eng. Perform. 27 (2018) 4345–4354.

[47] M. Michálek, K. Bodišová, M. Michálková, J. Sedláček, D. Galusek, Alumina/MWCNTs composites by aqueous slip casting and pressureless sintering, Ceram. Int. 39 (2013) 6543–6550.

[48] J. Sun, L. Gao, X. Jin, Reinforcement of alumina matrix with multi-walled carbon nanotubes, Ceram. Int. 31 (2005) 893–896.

[49] J. Gong, J. Wu, Z. Guan, Examination of the indentation size effect in low-load vickers hardness testing of ceramics, J. Eur. Ceram. Soc. 19 (1999) 2625–2631.

[50] R. Demichelis, Y. Noel, B. Civalleri, C. Roetti, M. Ferrero, R. Dovesi, The vibrational spectrum of α-AlOOH diaspore: an ab initio study with the CRYSTAL code, J. Phys. Chem. B 111 (2007) 9337–9346.